V. G. Chapin
Associate Professor
Department of Aerodynamic Energetic and Propulsion,
Institut Supérieur de l'Aéronautique et de l'Espace (ISAE),
Université de Toulouse,
Toulouse 31000, France
e-mail: vincent.chapin@isae.fr

E. Benard
Associate Professor
Department of Aerodynamic Energetic and Propulsion,
Institut Supérieur de l'Aéronautique et de l'Espace (ISAE),
Université de Toulouse,
Toulouse 31000, France
e-mail: emmanuel.benard@isae.fr

Active Control of a Stalled Airfoil Through Steady or Unsteady Actuation Jets

The active control of the leading-edge (LE) separation on the suction surface of a stalled airfoil (NACA 0012) at a Reynolds number of 10^6 based on the chord length is investigated through a computational study. The actuator is a steady or unsteady jet located on the suction surface of the airfoil. Unsteady Reynolds-Averaged Navier–Stokes (URANS) equations are solved on hybrid meshes with the Spalart–Allmaras turbulence model. Simulations are used to characterize the effects of the steady and unsteady actuation on the separated flows for a large range of angle of attack ($0 < \alpha < 28$ deg). Parametric studies are carried out in the actuator design-space to investigate the control effectiveness and robustness. An optimal actuator position, angle, and frequency for the stalled angle of attack $\alpha = 19$ deg are found. A significant increase of the lift coefficient is obtained (+84% with respect to the uncontrolled reference flow), and the stall is delayed from angle of attack of 18 deg to more than 25 deg. The physical nonlinear coupling between the actuator position, velocity angle, and frequency is investigated. The critical influence of the actuator location relative to the separation location is emphasized.
[DOI: 10.1115/1.4030483]

1 Introduction

The high applicative value of airfoils allowing large maximum lift coefficient and stall angle has been well known for many years in aeronautical and nonaeronautical applications [1]. Numerous passive design solutions have been proposed through geometry modifications such as multi-element airfoils with slat and flap systems, Krueger slats, and nose-tails [2]. These solutions are well proved but they are usually associated with mechanical systems adaptable to various flight conditions and therefore they are inherently heavy and costly. New, more flexible technologies are therefore called for if they can demonstrate equal or better overall performance, robustness, and adaptability to various flow conditions, while decreasing the weight penalty and complexity at a given level of reliability and security.

Today, with technological progress in micromechanical and fluidic systems and simultaneous improvements, to our knowledge on the field of control and stability of unsteady flows, it has become possible to investigate new solutions. Various technologies are under development and numerous actuators have been investigated in the literature (electrostatic, magneto-electrostatic, piezoelectric, and plasma systems [3–6]). These new solutions are based on passive, active, or adaptative control through mechanical or fluidic actuators [3] and they generate steady or unsteady effects on boundary conditions.

This paper focuses on those fluidic actuators able to generate steady or unsteady blowing and suction (continuous, synthetic, and pulsed jet actuators) on an airfoil. The basic idea is to add mean or fluctuating momentum into the flow in order to increase aerodynamic wing efficiency by controlling or modifying separated flows. It will be seen that the actuation should be implemented on the airfoil at the most appropriate location, scale, time, and phase, so that aerodynamic performance is increased through a higher maximum lift coefficient, and/or a larger range of angle of attack.

Contributed by the Fluids Engineering Division of ASME for publication in the Journal of Fluids Engineering. Manuscript received February 19, 2014; final manuscript received February 17, 2015; published online June 9, 2015. Assoc. Editor: Feng Liu.

The problem of optimizing actuation is complex because each actuator adds a significant number of parameters, thus increasing the number of possible solutions. Much more work is needed to improve our knowledge of these fluidic active systems, identify solutions, and find the most effective options.

Previous research investigations have been carried out experimentally [7–11] and numerically [10–16]. Seifert et al. [7] have shown experimentally that introducing two-dimensional periodic oscillations into a turbulent boundary layer enables it to resist larger adverse pressure gradients without separating. They also explain that the flow complexity requires extensive future investigation accompanied by numerical simulation targeted at the extraction of the leading parameters. Darabi and Wygnanski [8,9] have studied time scales of the phenomenon and found an optimal excitation frequency of $F^+_{\text{opt}} \approx 1.5$. Within the context of separation control with a dielectric barrier discharge plasma actuator at the leading edge of a thick airfoil (NACA 0021), Corke et al. [10,11] have shown that URANS results are consistent with experiments. Wu et al. have demonstrated the ability of two-dimensional URANS computations to simulate turbulent flow over an airfoil at poststall angles of attack and have shown that massively separated unsteady flows can be controlled by periodic blowing-suction near the leading edge, even at low level power input [12]. Duvigneau et al. [13–15] have run URANS simulations and studied the actuator location effect on a NACA 0012 airfoil. They have identified some optimal parameters, where the synthetic jet postpones the airfoil stall from 19 deg to 22 deg with maximum lift increasing by 34%. Huang et al. [16] have coupled steady RANS simulations and genetic optimization to search for optimal parameters for separation control with two actuators.

The interaction of actuators with the base flow is dependent on a large number of flow, geometry, and actuator parameters. The main parameters of the airfoil flow are the chord-based Reynolds number, the flow angle of attack, and the airfoil shape. For actuators, relevant parameters are location x_j, diameter d_j, momentum (square velocity for a jet), and direction of this momentum θ_j. If jet actuators are unsteady, one more parameter is their frequency f_j and the time profile of actuation (synthetic, pulsed, etc.). The role of the actuator's location will be the main focus of this paper, using the flexibility of numerical simulations of any

configurations for which experiments would be a more time consuming and costly option.

Separation control through steady blowing or steady suction is well established [1] and it probably finds its roots in 1904, with the pioneering work of Prandtl [17]. More recently, it has been demonstrated that unsteady forcing can be more cost-effective than steady forcing in delaying separation and enhancing aerodynamic performance [3]. It has also been shown that the spectral content of unsteady actuators may be of particular importance for the increase of the control authority [18].

The objectives of this paper will be to investigate flow control strategies around stalled-airfoils through local steady or unsteady forcing with actuators of continuous, synthetic, or pulsed jet types. Extended parametric studies will be used to extract the main flow parameters responsible for the separation control effectiveness and to define the best parameters for optimal control authority. Comments on physical mechanisms related to the actuation will also be put forward.

2 Numerical Setup and Physical Modeling

In this section, the main elements of the computational methodology flow solver characteristics, physical models, and the limitations are described. The URANS are resolved on hybrid meshes with a structured mesh region around the airfoil and an unstructured mesh region to complete the computational domain (Figs. 1 and 2). Conformal or nonconformal interfaces between the different mesh regions have been used.

2.1 Physical Model and Computational Method. FLUENT 6.3.26 was used to solve the URANS [19]. The two-dimensional incompressible Navier–Stokes equations are considered. The solver is based on a finite volume method for spatial discretization of all the transport equations. Second-order spatial and temporal numerical schemes were used in all the simulations. As is commonly proposed for low-speed external aerodynamics, simulations are based on the segregated solver with the Spalart–Allmaras turbulence model.

The resolution of the URANS was performed by considering a characteristic time scale t^* of the flow. For simulations of the reference case without control, the time scale was chosen as $t^* = c/V_\infty$ and for the controlled cases the time scale was chosen as $t^* = \min(1/f_j,\ c/V_\infty)$. The time step was chosen through the relation $t^*/\Delta t = 20$ in all cases. The independence of the results with respect to the time step used was checked in a study with a smaller step, $t^*/\Delta t = 40$, but no significant differences have been noted. The simulation time for appropriate convergence, in the worst case, was $T/t^* = 90$ and consequently, all simulations were extended up to $T/t^* = 180$ (Fig. 14).

As far as the boundary conditions were concerned, no-slip boundary condition on the airfoil surface, pressure outlet boundary condition, and velocity-inlet boundary condition on other flow domain frontiers were applied. The actuator has been modeled through a velocity-inlet boundary condition on the airfoil surface.

2.2 Turbulence Modeling. Although determination of laminar–turbulent transition effect on flow control is in general an important issue, in the current study, the influence of transition is supposed to be small. Indeed, the base flow of interest is essentially dominated by an adverse pressure gradient on the suction surface, thus making the flow unstable and prone to switch over a short length from the leading edge to a turbulent state. Therefore, it was decided to use a fully turbulent simulation for all parts of the flow, at the target medium Reynolds number range. This strategy is also based on the fact that systematic use of transition models in generic flow solver is not yet a well-established approach and lacks systematic validation. Hence, no transition models have been used in the following RANS simulations.

From the turbulence modeling point of view, the turbulence model of Spalart–Allmaras with standard coefficient values was used [20]. Preliminary simulations were done to evaluate the influence of turbulence models on flows at high angles of attack, with and without control. No significant improvements were detected with a two-equation turbulent model such as the k-ω SST, which is one of the most accepted in external aerodynamics studies. Moreover, the choice of the Spalart–Allmaras model is particularly relevant for parametric and optimization studies because it is a robust and low cost model.

2.3 Mesh Issues. GAMBIT 2.3.16 was used for mesh generation [21]. The mesh topology used is hybrid with an inner region around the airfoil and an outer region to extend the flow domain far from the airfoil to reduce the influence of boundary conditions on the numerical results (see Figs. 1 and 2) The inner region is a structured C-mesh for a better resolution of boundary layers, wakes, and separation shear layers. The outer region is unstructured to limit the total number of mesh points and computing time. This mesh topology presents high flexibility and good mesh quality control around the airfoil, and in the regions of interest (boundary layers, airfoil wake, and jet actuator).

In order to evaluate the ability of the numerical approach to predict the flow around airfoils with and without control, grid refinement and boundary condition studies have been carried out. To obtain more details, the simulation methodology was previously validated for separated flows using comparisons with experimental data [22].

The influence of boundary conditions on numerical results was tested through variation of the domain size. It was shown that a distance of 15 chords between the boundaries and the airfoil was sufficient to ensure convergence of aerodynamic coefficients (lift and drag) to less than 1% of their asymptotic value. All meshes used in this paper have the same overall size of 40×40 chord

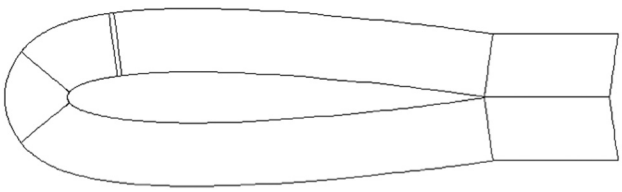

Fig. 1 Mesh topology with structured blocks around the airfoil

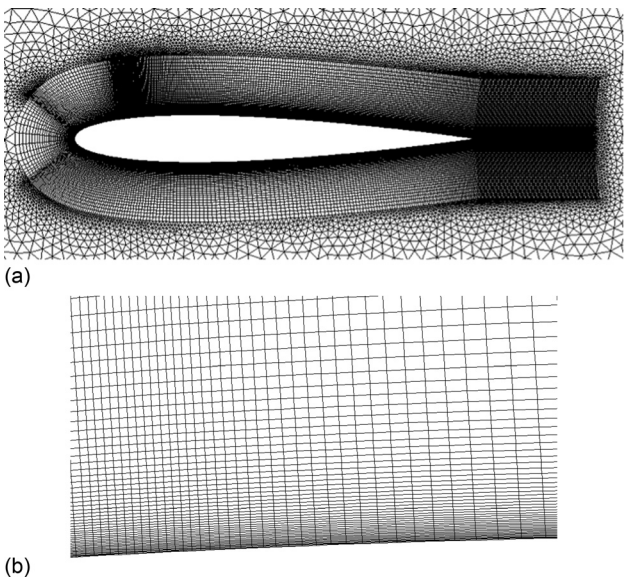

Fig. 2 (*a*) A typical hybrid mesh around the airfoil with a jet located at $x_j/c = 12\%$ and (*b*) zoom on the boundary layer mesh along the airfoil surface

length. The decision to fix the number of grid points in the jet at ten was validated as a sufficient description of the actuator influence on the main flow.

To evaluate the grid independence, four different hybrid meshes with increasing density were generated. Their respective characteristics are described in Table 1. The prediction of aerodynamic coefficients on these meshes is summarized in Table 2. All numerical simulations were done through RANS modeling when actuation and predicted solutions were steady and through time accurate URANS modeling when the actuation or the predicted solutions were unsteady. For time accurate solutions, time-averaged aerodynamic coefficients were considered. The averaging was done over ten periods for each solution.

2.4 Mesh Requirements and Validations. Preliminary numerical simulations were run on the NACA 0012 airfoil at a chord-based Reynolds number $\mathrm{Re} = 10^6$ in order to evaluate the mesh required to obtain accurate predictions of the main flow features. This mesh refinement study was focused on the accurate prediction of boundary layers, wakes, and shear layers because they are the key flow features that determine the separated zone on the suction side, at a high angle of attack.

For the Reynolds number of this study, observed flow regimes following Wu et al. [12] analysis are steady regimes at a low angle of attack and unsteady ones with vortex shedding at a high angle of attack. The vortex shedding is related to the LE separation and the resultant stall of the airfoil. This is the main physical phenomenon of interest, which will be targeted by the control strategy implemented in this study. To assess the relevance of simulations based on time accurate URANS modeling for studying the control of leading-edge flow separation, it should first be shown that this modeling approach is able to capture the main physical phenomenon to be controlled. Also, mesh refinement studies and validations through comparisons with experimental data were done and are presented in Secs. 2.5 and 2.6.

In Figs. 3 and 4, the lift coefficient asymptotic convergence is presented for various angles of attack on the four meshes (R_0, R_1, R_2, and R_3), as described previously in Table 1. When the flow solution is unsteady, at high angle of attack, the simulation time is increased to obtain periodic convergence of the lift and drag coefficients. Results reveal a very small influence of the mesh in the linear part of the curve for low angles of attack, from 0 deg to 12 deg (Fig. 3). As may be anticipated from previous studies [10], around the stall region, from 14 deg to 20 deg, results show a greater influence of the mesh on the predicted lift coefficient versus the angle of attack (Fig. 4). The stall angle found is 16 deg for all meshes. The lift convergence with mesh refinement is obtained for all angles of attack except 17 deg and 18 deg, just beyond stall (Fig. 4). For all other angles of attack, the flow solution is steady. Lift and drag coefficients values are given in Table 2 for each mesh. The differences in lift and drag coefficients between meshes R_0 and R_1 are less or equal to 1% except for an angle of attack just after stall (17 deg and 18 deg). Based on this mesh analysis, the mesh R_1 was adopted for the rest of the study detailed in this paper.

2.5 NACA 0012 Without Control. The validations and comparison of experimental and numerical data are always a difficult issue. It is far more difficult when considering an unsteady separated flow regime because of the high sensitivity to small changes in flow conditions. In Fig. 5, experimental data corresponding to various flow conditions and Reynolds numbers are represented in order to illustrate the sensitivity of the flow at high angle of attack [23–26]. The high dependency of the maximum lift coefficient and stall angle on the Reynolds number is well illustrated. In fact, the stall behavior also depends on numerous parameters of the test facility, such as the wind-tunnel wall, wing aspect ratio, three-dimensional effects, transition location, and Mach number, which are not always fully documented. The general trend from Fig. 5 is that the maximum lift coefficient and the stall angle both increase from 0.85 to 1.5 and from 11 deg to 16 deg, respectively, for Reynolds numbers increasing from 3.3×10^5 to 3×10^6.

In the light of this high sensitivity, the objective of the paper is to obtain a relevant qualitative description of the main flow features that play an important role in stall control. When present computations are compared to experimental results at various Reynolds numbers, differences appear, as may be seen in Fig. 6, but the overall trend is qualitatively in agreement with the experiments. At low angles of attack, the flow is attached to both sides of the airfoil. At medium angles of attack, flow separates on the suction side from the trailing edge. When the angle of attack is increased, the separation point moves upstream smoothly to half chord and then faster toward the leading edge when stall occurs. As frequently observed, numerical simulations overestimate the maximum lift coefficient and stall angle values. Numerical

Table 1 Grid parameters of the meshes (R_0, R_1, R_2, and R_3)

	R_0	R_1	R_2	R_3
Grid points	80,000	30,000	13,000	5000
Wall $y+$	1.0	1.0	1.0	3.0
n_ξ	800	400	200	100
n_η	80	40	20	10
n_{jet}	10	10	10	5

Table 2 Grid dependence of the aerodynamic coefficients (C_l and C_d)

	R_0		R_1		R_2		R_3	
α	C_l	C_d	C_l	C_d	C_l	C_d	C_l	C_d
0	0.00	0.012	0.00	0.012	0.00	0.012	0.00	0.014
2	0.20	0.012	0.20	0.012	0.20	0.013	0.20	0.014
4	0.39	0.013	0.40	0.013	0.40	0.014	0.40	0.016
6	0.59	0.015	0.59	0.015	0.59	0.016	0.59	0.019
8	0.78	0.017	0.78	0.017	0.78	0.019	0.77	0.024
10	0.95	0.021	0.96	0.021	0.95	0.023	0.93	0.031
12	1.12	0.025	1.12	0.026	1.11	0.028	1.08	0.040
14	1.26	0.033	1.26	0.033	1.24	0.037	1.19	0.052
16	1.34	0.047	1.33	0.048	1.31	0.053	1.24	0.077
18	1.15	0.115	1.23	0.141	1.22	0.152	1.08	0.134
19	0.89	0.182	0.90	0.180	1.00	0.278	0.98	0.178
20	0.79	0.234	0.80	0.234	0.96	0.317	1.06	0.134

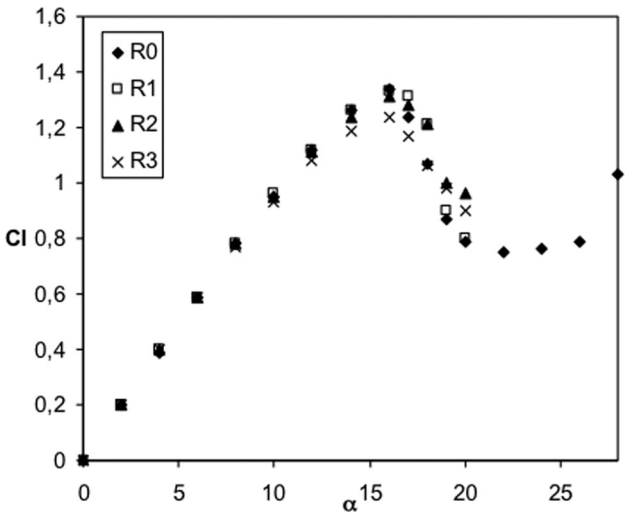

Fig. 3 Grid dependence of the mean lift coefficient versus angle of attack, $\mathrm{Re} = 10^6$

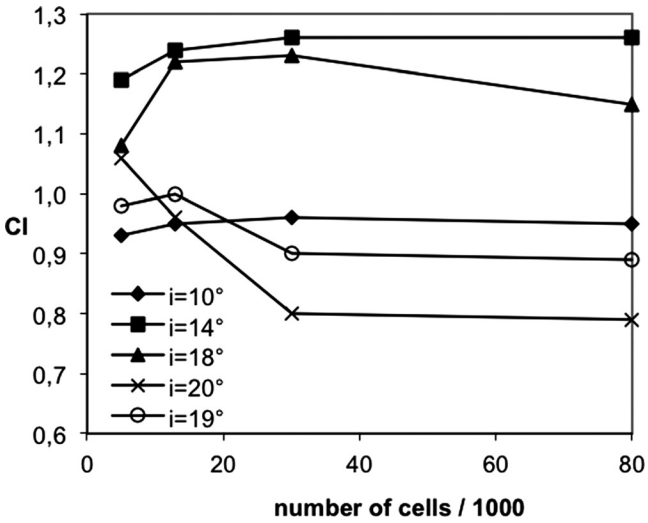

Fig. 4 Mesh refinement convergence study at various angles of attack for mean lift coefficient

simulations at $Re = 10^6$ predict a stall angle at around 16 deg, while corresponding experiments of Critzos et al. [24] indicate 12 deg at $Re = 5 \times 10^5$ and 14 deg at $Re = 1.8 \times 10^6$ but it may be observed that Ericsson and Reding [27] suggest stall at a 16 deg angle, at $Re = 1.34 \times 10^6$.

Despite the known dispersion of the lift coefficient in the stall region, numerical predictions are in reasonable agreement with experimental data in the pre- and post-stall regions. Where the main flow features relevant to flow control at high angles of attack are concerned, the migration of flow separation with the angle of attack is qualitatively well predicted (Fig. 6(*b*)). The stall behavior when the separation point moves rapidly forward to leading edge at stall angle is also predicted (Fig. 6(*b*)).

2.6 Parameters of the Flow Control Configuration. After the validation of the numerical methodology, the parameters of the chosen controlled configurations have to be defined. Numerical experiments were carried out on a NACA 0012 with a chord Reynolds number ranging from 10^6 to 3×10^6, in an incompressible regime. The jet actuator was added to the airfoil surface to implement blowing and/or suction in the boundary layer through a thin slot of width d_j. This actuator was modeled by a velocity-inlet boundary condition without taking into account of the internal pipe flow. The jet width ratio d_j/c was chosen to be 1%. Based on previous studies [13–16,28], the actuator location was chosen to be on the suction side in the range $0.05 < x_j/c < 0.5$, where separation of the boundary layer takes place in stall conditions. An exception to this was during the parametric study when the actuator location x_j/c was fixed to 12% of the airfoil chord. Three kinds of jet actuation were tested: the continuous jet, which creates a steady blowing at jet velocity V_j and two unsteady jets (synthetic or pulsed). The synthetic jet is a zero net mass flow jet, with suction and blowing half periods. In its most general form, the jet velocity can be expressed as follows:

$$V_j(t) = V_{jm} + V_{jf} \times f(f_j, t) \tag{1}$$

with $f(f_j, t)$ is the periodic function of time. The typical synthetic jet has a zero mean velocity component ($V_{jm} = 0$) but, in general, it may be useful to mix a steady and an unsteady component to the jet velocity as implemented by Seifert et al. [7]. In the present paper, the function $f(f_j, t)$ is sinusoidal with a zero mean for the synthetic jet and square with a nonzero mean for a pulsed jet as shown in Fig. 7.

All parameters of the actuation design-space are summarized in Fig. 8. They are the actuator location x_j, width d_j, velocity vector (V_j, θ_j), and frequency f_j, when unsteady mode is chosen. For the pulsed jet, the duty-cycle (DC) is always fixed to 0.5.

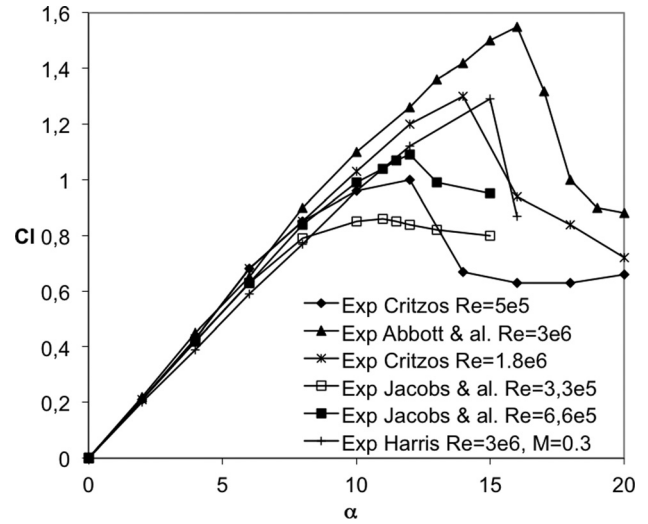

Fig. 5 Lift versus angle of attack experimental results on NACA 0012

3 Results and Discussion

3.1 Steady and Unsteady Jet Control. One preliminary objective was to compare numerical predictions with existing results of flow control. It is known from previous experimental and numerical experiments [7,13–16,28,29] that nearly tangential steady and/or unsteady blowing in the LE region of an airfoil at a poststall angle of attack may result in an increase in lift coefficient and a decrease in drag coefficient. It has been shown that this is related to the decrease of the separation zone on the suction side of the airfoil. As a prerequisite, in order to evaluate the ability of the numerical methodology to predict results similar to previous experiments and numerical simulations, a first series of numerical experiments was performed with actuator parameters defined in Table 3.

Results presented in Fig. 9 show that at poststall conditions, for an angle of attack greater than 15 deg, all controlled flows postponed the lift drop to a higher angle of attack by increasing the lift coefficient and the stall angle. This result is consistent with previous experiments of Gilarranz et al. [28] and numerical predictions by Rosas [30] and Duvigneau et al. [15]. In this study, the maximum forcing magnitude of the unsteady actuator (synthetic or pulsed) is set to the magnitude of the steady actuator. Set to this arbitrary level of actuation, the steady blowing of the continuous jet seems slightly superior to a synthetic or pulsed jet but the differences are small and not in favor of a continuous jet at all angles of attack. The maximum lift increase is $\Delta C_l = 0.7$ and it corresponds to a poststall angle of attack greater or equal to 20 deg. This lift increase is consistent with the Gilarranz experiment ($\Delta C_l = 0.6$) [28]. Hence, it is seen that, in this particular case, with an actuator frequency $F_j^+ = 1$, unsteady actuators are nearly as efficient as steady ones.

Figures 10 and 11 illustrate that the control effectiveness is dependent on the existence and location of flow separation and hence increases with the angle of attack for poststall angles of attack. At an angle of attack of 16 deg, with an actuator located at $x_j/c = 12\%$, the separation point on the suction side is postponed from $x_s/c = 61\%$ to $x_s/c = 69\%$ and results in a negligible increase of the lift coefficient ($\Delta C_l = 0.02$). For an angle of attack of 18 deg, with an actuator location at $x_j/c = 12\%$, the separation point initially located at $x_s/c = 21\%$ is postponed to $x_s/c = 45\%$ and a larger increase of lift coefficient is observed ($\Delta C_l = 0.2$).

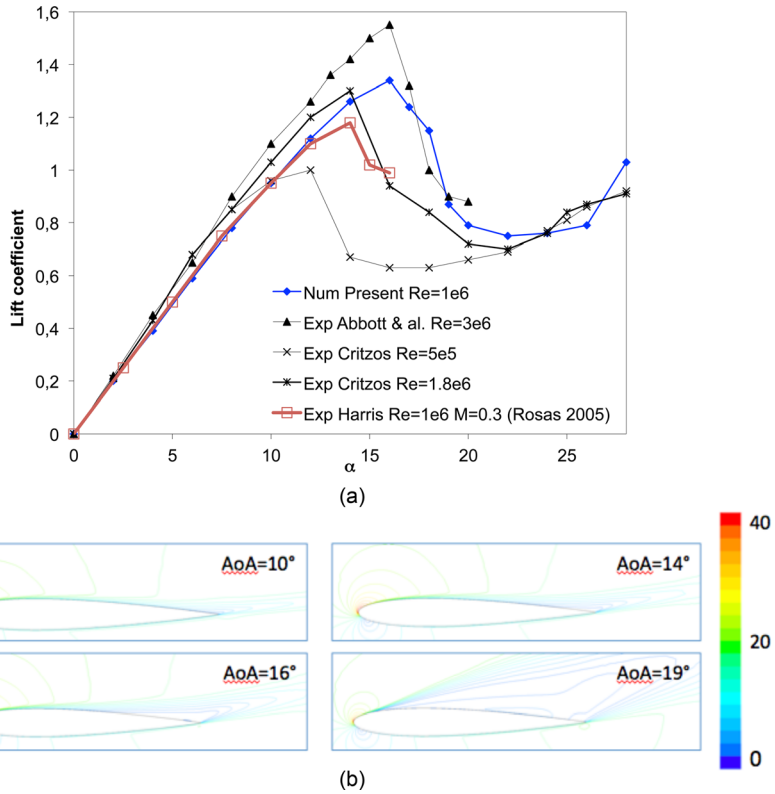

Fig. 6 (*a*) Comparison of experimental and numerical results on lift coefficient versus angle of attack on NACA 0012 and (*b*) velocity magnitude at angle of attack (AoA) = 10 deg, 14 deg, 16 deg, and 19 deg

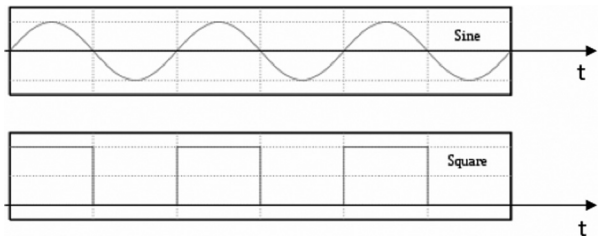

Fig. 7 Periodic function of time $f(f_j, t)$ of the actuator for synthetic and pulsed jet

From these results with a fixed actuator location, nothing can be said about the role of the actuator position relative to the separation location. This effect will be analyzed in Sec. 3.2 at fixed angle of attack $\alpha = 19$ deg in poststall conditions.

3.2 Parametric Study of the Synthetic Jet Actuation at $\alpha = 19$ deg. It was seen in Sec. 3.1 that the effectiveness of the control was highly dependent on the angle of attack. This is related to the fact that when the angle of attack increases, the separation zone becomes more extended, hence, the distance between the separation point and the actuator changes because the actuator location was fixed to $x_j/c = 12\%$. This first study, with a fixed actuator location, was done to make comparisons with the experiment of Rosas [30] and to validate our numerical approach.

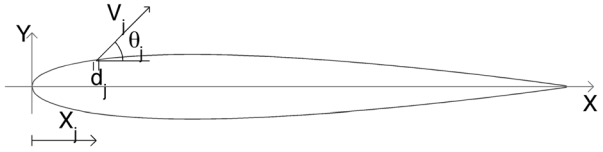

Fig. 8 Airfoil and the actuator design-space (x_j/c, d_j/c, V_j, and θ_j)

The change of actuator location is not easy to implement in an experiment, for reasons previously outlined, but neither is it in a numerical simulation because of programming limitations and mesh generation automation. To overcome this difficulty, the simulation platform VLab, developed for this study, has been extended to take into account the actuator displacement along the suction side of the airfoil. The displacement of the actuator is automatically taken into account by the platform, and the mesh is automatically adapted and refined around the actuator for an accurate modeling of high flow gradients in the actuator region (Fig. 2). The investigation of the effectiveness of separation control at a given poststall angle of attack was done through one-dimensional parametric studies of the entire actuator design-space (x_j, V_j, θ_j, and f_j), including the actuator location. For this study, each parameter is varied separately and all the nonvarying dimensionless parameters of significance are fixed at their nominal value ($d_j/c = 1\%$, $x_j/c = 12\%$, $V_j/V_\infty = 2$, $\theta_j = 15$ deg, and $F_j^+ = 1$). This was done for a poststall angle of attack ($\alpha = 19$ deg), where the control authority was high as shown in Sec. 3.1.

3.3 Actuator Location. First of all, the actuator location was studied as the key parameter to understand the role played by the distance between the separation point and the actuator location. Figures 12(*a*) and 13 and Table 4 illustrate a first key result of this study: the actuator position, which maximizes the effectiveness

Table 3 Actuator reference parameters

	d_j/c (%)	x_j/c (%)	V_j/V_0	θ_j (deg)	F_j^+
Continuous jet	1	12	2	15	—
Synthetic jet	1	12	2	15	1
Pulsed jet	1	12	2	15	1

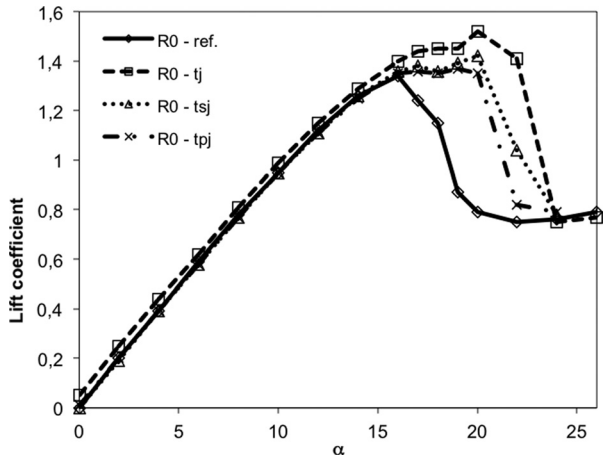

Fig. 9 Lift coefficient versus angle of attack, Re = 10^6. (ref.) reference case without control, (tj) tangential continuous jet, with $V_j/V_0 = 2$, $\theta_j = 30$ deg and $x_j/c = 12\%$ (tsj) tangential synthetic jet, with $V_j/V_0 = 2$, $\theta_j = 30$ deg and $x_j/c = 12\%$, $f_j = 15$ (tpj) tangential pulsed jet. with $V_j/V_0 = 2$, $\theta_j = 30$ deg and $x_j/c = 12\%$, $f_j = 15$, DC = 0.5.

of the control, is not near the separation point ($x_j/c = 12\%$ with $x_s/c = 8\%$ for present angle of attack $\alpha = 19$ deg) but is more downstream ($x_j/c = 40\%$). Table 4 shows that with an actuator located at $x_j/c = 40\%$, the separation point is moved in the downstream direction by 54% of the airfoil chord and by only 26% for the actuator located near the separation point $x_j/c = 12\%$. A more detailed analysis of Fig. 12(*a*) shows a first area from $x_j/c = 4\%$ to 15%, where the lift increases and the separation point moves downstream. In a second area, from $x_j/c = 15\%$ to 40%, the lift increases more slowly before dropping down suddenly for $x_j/c = 45\%$ at which the separation point comes back toward the LE of the airfoil as may be seen on Fig. 13.

The optimal location found, $x_j/c = 40\%$ to maximize the lift increase, is interesting because it shows that, on contrary to what is generally stated without a detailed analysis of the actuator location, the best location for the actuator seems not to be near the separation point but farther downstream implying that some actuator locations have a global nonlinear effect on the flow separation region. In this case, it shows that a critical actuator location exists on the wall of the suction surface (here between $x_j/c = 40\%$ and 45%). Upstream of this location, the control effect is maximized (Fig. 13(*c*)) and downstream of it the control becomes ineffective (Fig. 13(*d*)).

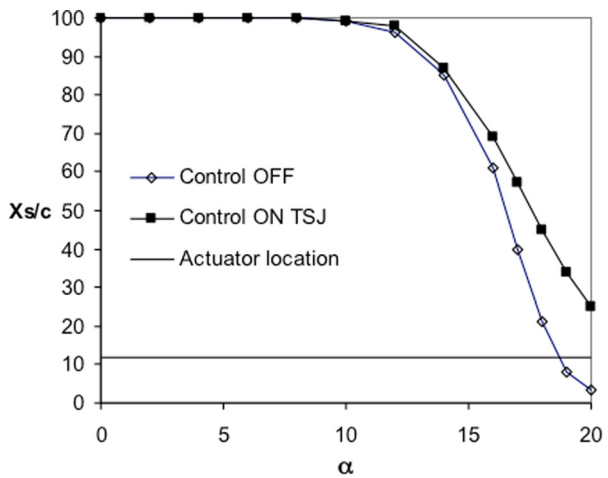

Fig. 10 Mean flow separation location versus angle of attack for tangential synthetic jet

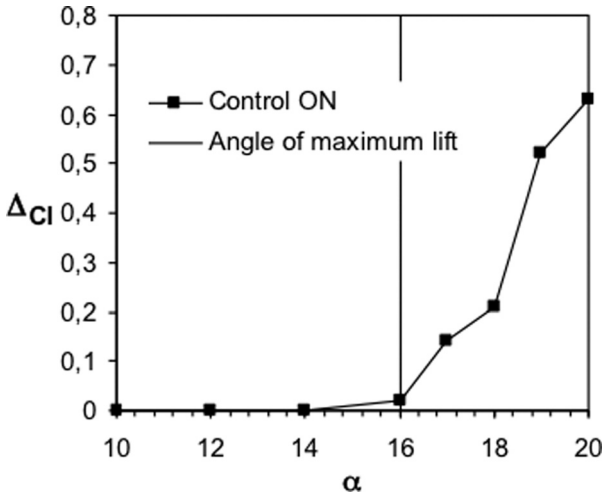

Fig. 11 Actuator effect on mean lift coefficient versus angle of attack

Another question investigated was the robustness of the residual separation region on the suction side near the trailing edge of the airfoil, when the actuator is located downstream at $x_j/c = 40\%$ (Fig. 13(*c*)). Additional simulations have been done with the actuator located at $x_j/c = 40\%$ in order to investigate any potential hysteresis effect. It was shown that if the control was turned off, the lift went down to its reference value, and if the control was turned on, the separated flow reattaches and the lift comes back to the control on value without any significant hysteresis effect. On the other hand, with the actuator located at $x_j/c = 45\%$ it was not possible to control the leading-edge flow separation on the suction side (Table 4 and Fig. 13(*d*)). In other words, the attached flow solution found with a synthetic jet was stable with a jet located at $x_j/c = 40\%$ but was not stable with a jet located at $x_j/c = 45\%$.

In Fig. 14, it can be seen that the reference flow without control converges to a steady solution. In the same figure, solutions with synthetic jet control located at $x_j/c = 10\%$, 40%, and 45% converge toward unsteady periodic solutions with a period equal to the jet period ($T_j = 1/f_j$). The steady nature of the reference flow without control is associated with a steady asymmetric vortex pair of opposite sign on the suction side of the airfoil as may be seen in Fig. 13. The unsteady nature of the efficiently controlled flow (actuator at $x_j/c = 10\%$, 40%) is associated with a single vortex on the suction side with periodic vortex shedding. The separation point on the suction side is farther downstream ($X_s/c = 32\%$ and 48%) than in the reference case ($X_s/c = 8\%$). The unsteady nature of the inefficiently controlled flow ($x_j/c = 45\%$) is associated with a vortex pair of opposite sign with periodic vortex shedding as seen in the uncontrolled case. The separation point on the suction side is nearly unchanged relative to the uncontrolled case ($X_s/c = 8\%$), but the mean lift is a little higher than the reference case value.

According to these results and applied to real cases, the maximization of mean lift at various angles of attack will rely on having a distribution of actuators along the suction surface that may be activated depending on the separation location. As illustrated in Fig. 10, another advantage of this multi-actuator configuration would be to increase the control effect and robustness by activating two or more actuators simultaneously to suppress completely the separation on the suction side of the airfoil or to adapt the control to variations in the environment such as wind gusts.

3.4 Actuator Velocity Vector. Another open question to be investigated was the influence of the synthetic jet angle. Rosas [30] investigated the influence of the actuator jet angle for nearly tangential configurations. His study shows that when the actuator jet angle increases from a nearly tangent value of 2 deg to 10 deg, the mean lift coefficient decreases and fluctuations of lift increase. Our parametric study shows that the best synthetic jet flow angle

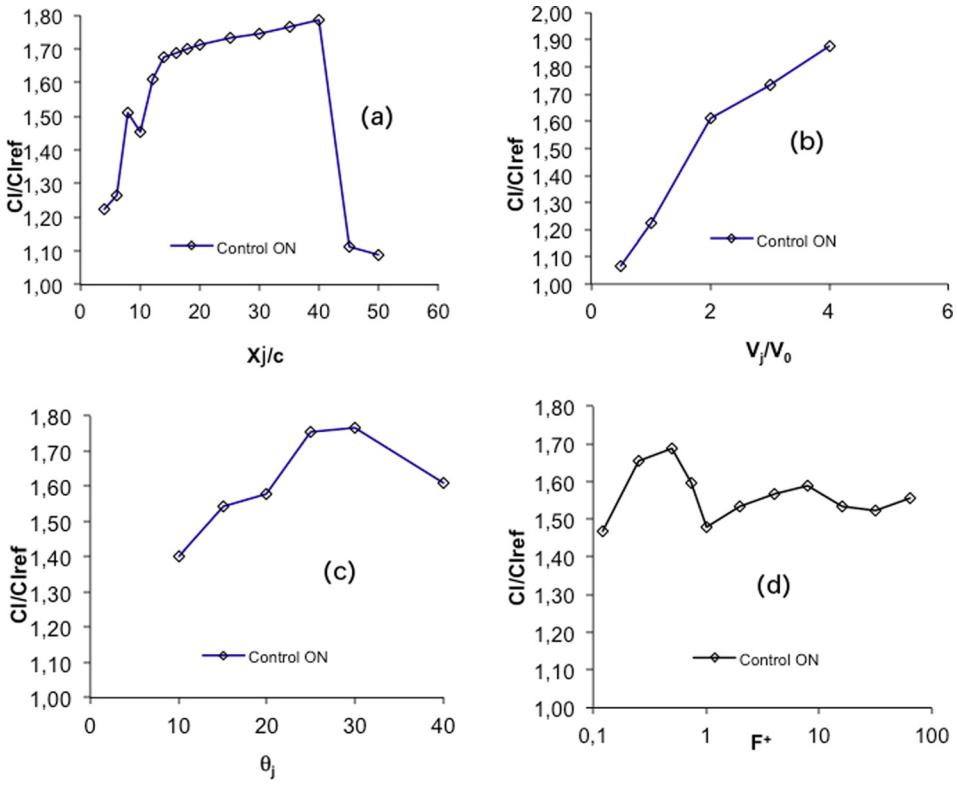

Fig. 12 Effects of the four synthetic jet actuator parameters (x_j/c, V_j, θ_j, and f_j) on the lift coefficient, $\alpha = 19$ deg: (*a*) actuator location x_j/c effect with $V_j/V_0 = 2$, $\theta_j = 30$ deg, and $f_j = 15$; (*b*) Actuator velocity magnitude V_j/V_0 effect with $x_j/c = 12\%$, $\theta_j = 30$ deg, and $f_j = 15$; (*c*) actuator velocity angle θ_j effect with $V_j/V_0 = 2$, $x_j/c = 12\%$, and $f_j = 15$; and (*d*) actuator frequency f_j effect with $V_j/V_0 = 2$, $\theta_j = 30$ deg, and $x_j/c = 12\%$

is neither tangential nor normal but intermediate, with a value around $\theta_j = 30$ deg (Fig. 12(*c*)). A similar result was found in the numerical study of Duvigneau et al. [14]. In Fig. 12(*b*), it may be seen that the jet velocity magnitude increase is correlated to the increase in the control efficiency. No saturation effect was observed for velocities as high as $V_j/V_\infty = 4$, but the slope decreases after $V_j/V_\infty = 2$.

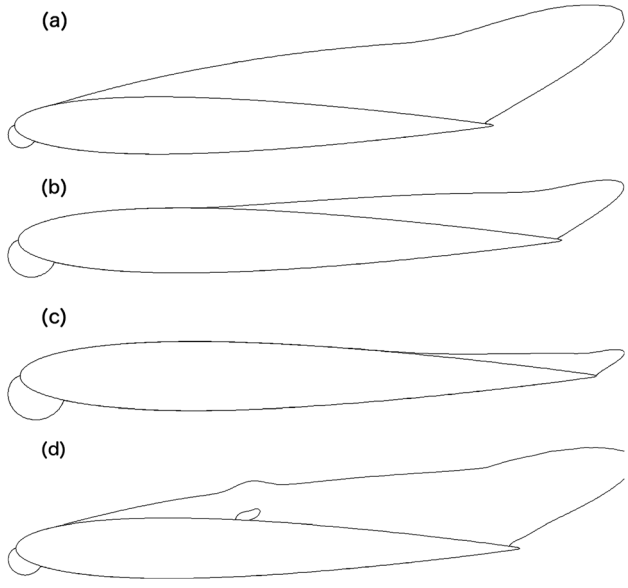

Fig. 13 Instantaneous streamlines with various actuator locations for $\alpha = 19$ deg: (*a*) control OFF, (*b*) control ON $X_j/c = 12\%$, (*c*) control ON $X_j/c = 40\%$, and (*d*) control ON $X_j/c = 45\%$

3.5 Actuator Frequency. The influence of the actuator frequency on the lift increase is a complex issue. It has been widely considered in control experiments and many length scales have been used in the literature without general consensus on an appropriate choice [31]. The difficulty is related to the fact that there are generally multiple natural frequencies present in the flow with potentially nonlinear interactions between each of them and the frequency of the actuator [31]. Here, it is found that, for the selected configuration, the more efficient nondimensional frequency $F_j^+$is approximately 0.5 (a travel of 0.5 airfoil chord at free stream velocity) in terms of lift enhancement over all the considered frequencies from 0.1 to 30. More precisely, the control effectiveness is slightly higher for nondimensional frequency values from around 0.5 within 0.25 to 0.75 but the control is rather effective for a large range of frequencies tested from 0.1 to nearly 30. This is consistent with previous findings by Seifert et al. [7], who observed an optimal behavior with $F+\equiv fL/V_\infty = O(1)$, where L is the length of the separated region.

3.6 Coupling Mechanisms in the Design-Space. For a given poststall angle of attack ($\alpha = 19$ deg), one-dimensional parametric

Table 4 Separation control effectiveness

α (deg)	X_{sOFF}/c (%)	X_j/c (%)	$(X_s - X_j)/c$ (%)	X_{sON}/c (%)	ΔX_s (%)	$\Delta C_l/C_l$ (%)
16	61	12	49	69	+8	+2
18	21	12	9	45	+24	+22
19	8	12	−4	34	+26	+61
19	8	20	−12	48	+40	+71
19	8	40	−32	62	+54	+79
19	8	45	−37	10	+2	+11

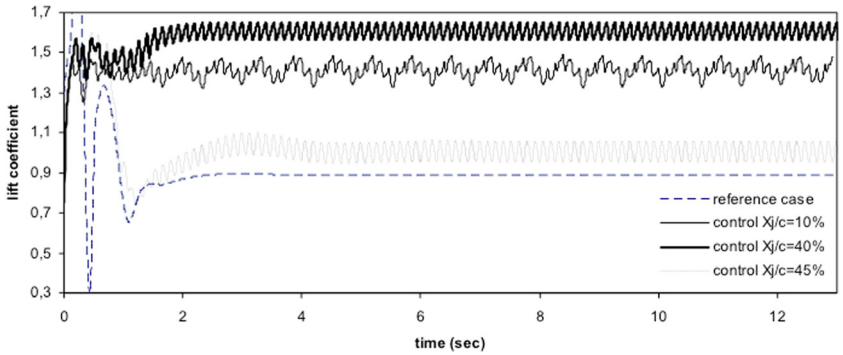

Fig. 14 Lift coefficient history with various actuator locations for $\alpha = 19$ deg

studies of the control authority versus actuator parameters (x_j, V_j, θ_j, and f_j) were reviewed in Secs. 3.3, 3.4, and 3.5. This was done in a very small part of the $\Re^4$ design-space with only four lines in it. In this four-dimensional design-space, a triplet was fixed to study the influence of the free parameter. In order to investigate further the nonlinear interactions between control parameters, response surfaces may be used to extract the coupling between two parameters and their influence on the aerodynamic performance [32]. To illustrate the usefulness of this method, three response surfaces were constructed to understand better the coupling mechanisms of the present flow control problem. Building on the data of Sec. 3.3, which clearly shows the highly nonlinear behavior of the jet location, we will now evaluate the coupling with the three other parameters of the jet actuation.

In Figs. 15–17, the coupling between the four parameters of the actuator (x_j, V_j, θ_j, and f_j) is illustrated. The range of the actuator parameters was chosen from the study of Secs. 3.3, 3.4, and 3.5.

In Fig. 15, the coupling between the jet location and jet angle is found to be low in the range tested. The influence of the velocity angle on the control efficiency versus the position of the actuator is noted only for nonoptimal, low (15 deg), and high (50 deg) values of the velocity angle, when the actuator is located near the separation point of the reference case ($x_j/c = 15$–20%). Given the discrete nature of the computed response surface, it seems that there is no local optimum but only a flat global optimum in the neighborhood of the computed optimal point $x_j/c = 40\%$ and $20\,\text{deg} < \theta_j < 40\,\text{deg}$. The most efficient actuator location decreases a little when the jet angle increases as may be seen for $\theta_j = 50$ deg and $x_j/c = 40\%$.

In Fig. 16, the coupling between the actuator position and frequency is clearly stronger than with the jet angle. The effectiveness of the control increases with jet location x_j/c before decreasing. The optimal location of the actuator is found to be $x_j/c = 35\%$ at all frequencies except for the three higher ones ($F_j^+ = 2$, 4, and 8) for which it is higher with $x_j/c = 45\%$. For a given location of the actuator, the frequency has a low influence on the effectiveness of the control except for the three high frequencies tested. High frequencies tested ($F_j^+ = 2$, 4–8) extend the range of efficiency of the actuator to 45% of the airfoil chord.

In Fig. 17, the coupling between the actuator velocity magnitude and location is presented for a jet angle of 15 deg and frequency $F_j^+ = 1$. For low values of the actuator location ($x_j/c = 32$–40%), the control authority increases in a linear fashion with the jet velocity magnitude. For high values of the actuator location ($x_j/c = 44$–50%), the jet velocity magnitude necessary for effective control increases and is superior to the freestream velocity. With a velocity ratio of two, the control is effective for $x_j/c < 56\%$. With a velocity ratio of one, the control is effective for $x_j/c < 44\%$.

These figures illustrate the benefit of using response surfaces to identify effectiveness of the control and coupling between each control parameters in the design-space.

3.7 Physics of Separation Control With a Synthetic Jet. The lift enhancement obtained through synthetic jet actuation on the suction surface has been identified and characterized in various configurations. The numerical simulation results may be used to enhance our understanding of the flow physics at play. To illustrate this point and gain insight into the stall control principle and

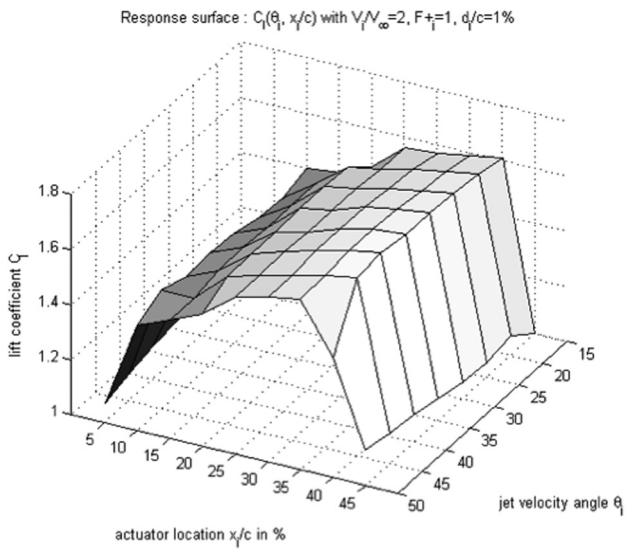

Fig. 15 Response surface of the lift coefficient $C_l(\theta_j, x_j/c)$

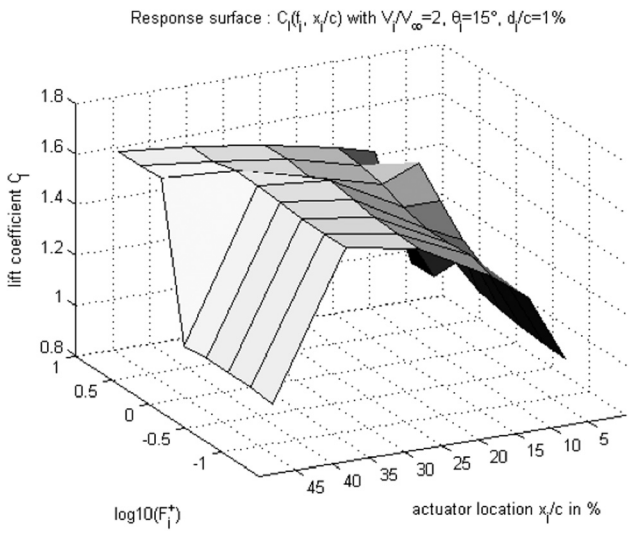

Fig. 16 Response surface of the lift coefficient $C_l(F^+_j, x_j/c)$

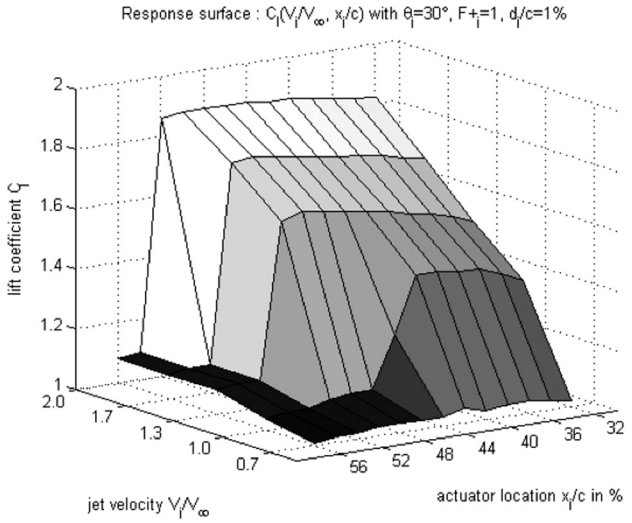

Fig. 17 Response surface of the lift coefficient $C_l(V_j/V_0, x_j/c)$

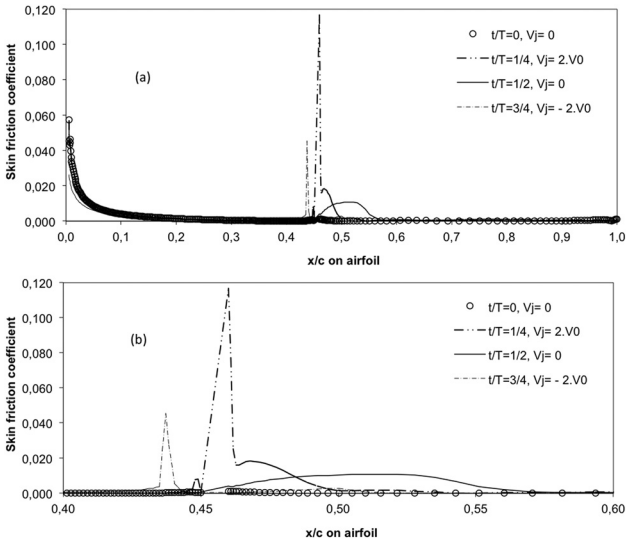

Fig. 19 Skin friction coefficient during one period of actuation of the synthetic jet: (*a*) skin friction along the airfoil suction surface and (*b*) zoom in the actuator region

effectiveness, the following configuration is studied in detail: a synthetic jet with $V_j/V_\infty = 2$, $\theta_j = 15$ deg, $F^+_j = 2$, and $x_j/c = 45\%$.

Figure 18 presents the time history of the jet velocity and the lift coefficient over one period of actuation. The first half period with positive jet velocity is the blowing phase of the control strategy. During this half period, the actuator transfers longitudinal momentum into the boundary layer. This added momentum is mainly oriented in the streamwise direction ($\theta_j = 15$ deg) and is localized in the initially separated region, i.e., at nearly zero wall skin friction. It results in a sharp increase of the wall skin friction as may be seen in Fig. 19. At the beginning of this half period (from 0 to $t/T = 1/4$), the first separation point is located at $x_s/c = 41\%$, upstream of the actuator and the wall skin friction increase located in the jet area. At the end of this half period ($t/T = 1/2$), the added momentum is diffused in the boundary layer and wall skin friction has decreased. During the second half period, the jet velocity becomes negative. This is the suction phase. It is seen in Fig. 19 that the previously injected momentum is convected in the downstream direction and diffused in the boundary layer. The mean lift coefficient presents a maximum value in the second half period. The separation point moves in the downstream direction to $x_s/c = 80\%$ at the end of the second half period. The time lag between the blowing phase maximum velocity of the jet actuation and the maximum lift coefficient may be seen in Fig. 18. Maximum actuation velocity is obtained at $t/T = 1/4$ (black symbol on velocity curve in Fig. 18) and the maximum lift coefficient is obtained at $t/T = 3/8$ (black symbol on lift curve in Fig. 18). The mean skin friction coefficient distribution

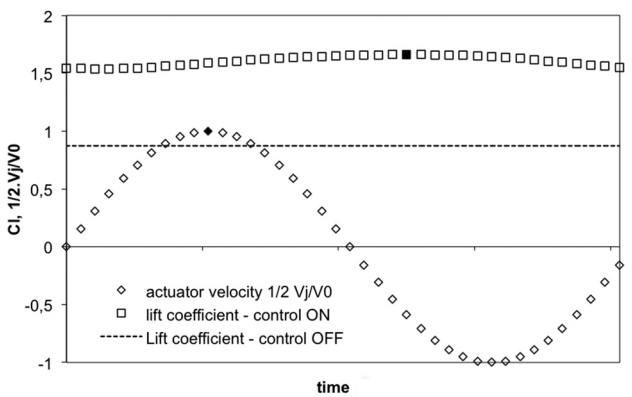

Fig. 18 Synthetic jet velocity and lift coefficient on one period of actuation

indicates that the mean separation point is located at $x_s/c = 71\%$ for this case.

The physical analysis of separation control through a synthetic jet may also be extended to the continuous jet mode, which is based on a continuous increase of the boundary layer energy to postpone the separation. The previous analysis also suggests this because only the blowing phase (first half period of the synthetic jet actuation) is useful for the control strategy. Also, in a future study, it would be useful to investigate in more detail pulsed jet control with a short duty-cycle to decrease the energy consumption of the actuation for a given lift increase.

4 Conclusion

The control of flow separation on the suction surface of a post-stall airfoil at a high Reynolds number through steady and unsteady jet actuators was studied by means of time accurate two-dimensional numerical simulations. Following validation studies and mesh independence simulations, results with a continuous and a synthetic jet were found to be consistent with previous experiments and numerical simulations. Tests with steady and unsteady control demonstrate significant improvements of lift coefficient ($+85\%$) with a jet located in the separation region ($x_j/c = 40\%$) and a postponed stall angle of attack from 16 deg to 22 deg with a jet located near the separation point ($x_j/c = 12\%$).

A detailed parametric study of the actuator design-space was carried out to investigate the influence of the actuator parameters on the control effectiveness and robustness, and to understand the behavior of the flow around a stalled airfoil with and without control. It was shown that nonlinear coupling in stalled airfoil flow control may take place between the base flow and the actuator flow. The nonlinear response of the flow to the actuator location and frequency for unsteady actuation has been identified and illustrated. Based on this flow response, it was shown that the optimal location of the actuator was not in the neighborhood of the separation point but farther downstream in the separated region on the suction surface of the airfoil. This result has been obtained assuming that the flow is dominated by two-dimensional unsteady flow phenomena.

In the future, these results should be investigated through experiments and/or numerical simulations with more advanced unsteady three-dimensional models such as detached eddy simulation and large eddy simulation. It is also planned to carry out

optimization studies to explore and describe in more detail the design-space of this flow control problem.

Acknowledgment

The authors would like to thank DGA/MRIS for its financial support of the present study.

Nomenclature

c = chord of airfoil (m)
C_d = drag coefficient
C_l = lift coefficient
C_p = pressure coefficient
d_j = actuator diameter (m)
DC = pulsed jet duty-cycle
f_j = actuator frequency (Hz)
F_j^+ = actuator nondimensional frequency $= f_j\, c/V_\infty$
LE = leading edge
n_{jet} = grid number of points in the tangential direction in the actuator jet
n_η = grid number of points in the normal direction
n_ξ = grid number of points in the tangential direction
T_j = actuator period (s)
TE = trailing-edge
u_τ = friction velocity (m/s)
V_j = actuator jet velocity (m/s)
V_{jf} = actuator jet fluctuation velocity (m/s)
V_{jm} = actuator jet mean velocity (m/s)
V_0 = freestream velocity (m/s)
x_j = actuator location (m)
x_s = separation point location (m)
X_{sOFF}/c = separation location with control OFF
X_{sON}/c = separation location with control ON
y^+ = wall viscous length scale $= y\, u_\tau/\nu$
α = angle of attack of the freestream velocity relative to the airfoil chord (deg)
Δt = time step (s)
Δx_s = distance between the separation point location with and without control (chord percentage)
θ_j = actuator jet velocity angle (deg)

References

[1] Fiedler, H. E., and Fernholz, H. H., 1990, "On Management and Control of Turbulent Shear Flows," Prog. Aeronaut. Sci., **27**(4), pp. 305–387.
[2] Gad-el-Hak, M., 1996, "Modern Developments in Flow Control," ASME Appl. Mech. Rev., **49**(7), pp. 365–379.
[3] Gad-el-Hak, M., 2000, *Flow Control: Passive, Active and Reactive Flow Management*, Cambridge University, London.
[4] Glezer, A., and Amitay, M., 2002, "Synthetic Jets," ARFM, **34**, pp. 503–529.
[5] Cattafesta, L. N., and Sheplak, M., 2011, "Actuators for Active Flow Control," ARFM, **43**, pp. 247–272.
[6] Corke, T. C., Lon Enloe, C., and Wilkinson, S. P., 2010, "Dielectric Barrier Discharge Plasma Actuators for Flow Control," ARFM, **42**, pp. 505–529.
[7] Seifert, A., Darabi, A., and Wygnanski, I., 1996, "Delay of Airfoil Stall by Periodic Excitation," J. Aircr., **33**(4), pp. 691–698.
[8] Darabi, A., and Wygnanski, I., 2004, "Active Management of Naturally Separated Flow Over a Solid Surface. Part 2. The Separation Process," J. Fluid Mech., **510**, pp. 131–144.
[9] Darabi, A., and Wygnanski, I., 2004, "Active Management of Naturally Separated Flow Over a Solid Surface. Part 1. The Forced Reattachment Process," J. Fluid Mech., **510**, pp. 105–129.
[10] Orlov, D. M., Apker, T., He, C., Othman, H., and Corke, T. C., 2007, "Modeling and Experiment of Leading-Edge Separation Control Using SDBD Plasma Actuators," AIAA Paper No. 2007-0877.
[11] Corke, T. C., Post, M. L., and Orlov, D. M., 2009, "Single Dielectric Barrier Discharge Plasma Enhanced Aerodynamics: Physics, Modeling and Applications," Exp. Fluids, **46**(1), pp. 1–26.
[12] Wu, J. Z., Lu, X. Y., Denny, A. G., Fan, M., and Wu, J. M., 1998, "Post-Stall Flow Control on an Airfoil by Local Unsteady Forcing," J. Fluid Mech., **371**, pp. 21–58.
[13] Duvigneau, R., and Visonneau, M., 2006, "Simulation and Optimization of Stall Control for an Airfoil With a Synthetic Jet," Aerosp. Sci. Technol., **10**(4), pp. 279–287.
[14] Duvigneau, R., and Visonneau, M., 2006, "Optimization of a Synthetic Jet Actuator for Aerodynamic Stall Control," Comput. Fluids, **35**(6), pp. 624–638.
[15] Duvigneau, R., Hay, A., and Visonneau, M., 2007, "Optimal Location of a Synthetic Jet on an Airfoil for Stall Control," J. Fluid Eng., **129**(7), pp. 825–833.
[16] Huang, L., Huang, P. G., LeBeau, R. P., and Hauser, T., 2004, "Numerical Study of Blowing and Suction Control Mechanism on a NACA 0012 Airfoil," J. Aircr., **41**(5), pp. 1005–1013.
[17] Fernholz, H. H., and Urzynicok, F., 2006, "Control of Weak and Strong Reverse-Flow Regions," *Control of Fluid Flow*, Springer, Berlin, pp. 1–44.
[18] Zhang, M. M., Zhou, Y., and Cheng, L., 2008, "Control of Post-Stall Airfoil Aerodynamics Based on Surface Perturbation," AIAA J., **46**(10), pp. 2510–2519.
[19] 2013, *FLUENT User's Guide and Reference Manuals*, Version 6.3.
[20] Spalart, P. M., and Allmaras, S. R., 1994, "A One-Equation Turbulence Model for Aerodynamic Flows," La Rech. Aérosp., **1**, pp. 5–21.
[21] 2003, *Gambit User's Guide and Reference Manuals*, Version 2.3.
[22] Chapin, V. G., Jamme, S., and Chassaing, P., 2005, "Viscous Computational Fluid Dynamics as a Relevant Decision-Making Tool for Mast-Sail Aerodynamics," Marine Technol., **42**(1), pp. 1–10.
[23] Abbott, V., and Doenhoff, S., 2005, *Theory of Wing Sections*, Dover Editions, New York, p. 123.
[24] Critzos, C. C., Heyson, H. H., and Boswinkle, R. W., 1955, "Aerodynamic Characteristics of a NACA 0012 Airfoil Section at Angles of Attack From 0 deg to 180 deg," Report No. NASA TN3361.
[25] Harris, C. D., 1981, "Two-Dimensional Aerodynamic Characteristics of the NACA0012 Airfoil in the Langley 8-Foot Transonic Pressure Tunnel," NASA Technical Memorandum No. 81927.
[26] Jacobs, E., and Sherman, A., 1937, "Airfoil Section Characteristics as Affected by Variations of the Reynolds Number," NACA Report No. 586, p. 231.
[27] Ericsson, P. M., and Reding, S. R., 1977, "Further Consideration of 'Spilled' Leading-Edge Vortex Effects on Dynamic Stall," J. Aircr., **14**(6), pp. 601–603.
[28] Gilarranz, J., Traub, L., and Rediniotis, O., 2002, "Characterization of a Compact, High Power Synthetic Jet Actuator for Flow Separation Control," AIAA Paper No. 2002-0127.
[29] Sosa, R., Artana, G., and Moreau, E., 2007, "Stall Control at High Angle of Attack With Plasma Sheet Actuators," Exp. Fluids, **42**, pp. 143–167.
[30] Rosas, C. R., 2005, "Numerical Simulation of a Flow Separation Control by Oscillatory Fluid Injection," Thesis report, Texas A&M University, College Station, TX.
[31] Raju, R., Mittal, R., and Cattafesta, L. N., 2007, "Towards Physics Based Strategies for Separation Control Over an Airfoil Using Synthetic Jets," AIAA Paper No. 2007-1421.
[32] Shyy, W., Papila, N., Vaidyanathan, R., and Tucker, K., 2007, "Global Design Optimization for Aerodynamics and Rocket Propulsion Components," Prog. Aerosp. Sci., **37**, pp. 59–118.